Blockage Mitigation via Curved Airy Beams in Near Field Terahertz Communications Beyond 6G

Md Hasibul Islam[1], Vitaly Petrov[2], Hichem Guerboukha[1]
[1]University of Missouri – Kansas City, Kansas City, MO, USA
[2]KTH Royal Institute of Technology, Stockholm, Sweden
Email: {hiqqd, hichem.guerboukha}@umkc.edu, vitalyp@kth.se

2025 IEEE 22nd Consumer Communications & Networking Conference (CCNC) | 979-8-3315-0805-0/25/$31.00 ©2025 IEEE | DOI: 10.1109/CCNC54725.2025.10975973

***Abstract*—The terahertz (THz) spectrum holds immense potential for advanced wireless communication systems due to abundant available bandwidth and high data rates. However, a major challenge in deploying THz systems is susceptibility to blockage, which can greatly impair signal propagation and negatively affect the reliability of the communication link. This paper focuses on applying self-accelerated beams for blockage mitigation at THz frequencies. These beams can follow curved trajectories as they propagate in free space. Trajectories can be engineered to overcome physical obstacles present in the beam path. As we show through extensive simulations, self-accelerated beams perform better than conventional Gaussian beams in terms of received power when obstacles are present. This approach offers new possibilities for reliable THz communications in practical deployment scenarios.**

***Index Terms*—THz spectrum, 6G, Beyond-6G, near-field communications, Airy beams, caustic beams, trajectory engineering.**

I. Introduction

The adoption of high-frequency terahertz (THz, 300 GHz–3 THz) bands is widely regarded as a key enabling technology for future wireless communications systems employed in sixth-generation (6G) networks and beyond [1]–[3]. Current experimental sub-THz testbeds have successfully demonstrated data transmission rates of several hundreds of Gbps [4] with a recent milestone achieving 1.44 Tbps [5]. The latter value already exceeds one terabit-per-second aim tentatively set as a target peak data rate for 6G [6].

Despite these promising advancements, many challenges remain and impede the widespread deployment of THz-based wireless communication systems. The *reliability* of wireless THz links is one of the major concerns. As free-space path loss (assuming omnidirectional antennas on both sides) increases quadratically with frequency, it becomes a critical limitation in the THz band. For example, a 1-meter link at 300 GHz may experience as much as 80 dB of losses. Hence, prospective THz links will rarely utilize omnidirectional (or even quasi-omni) in next-generation wireless networks. A standard strategy to counter these high losses is to use highly directional "pencil-like" beams generated by high-gain antennas [7]. The antenna gains can counterbalance the spreading losses: when antenna gains and transmit powers are carefully selected, multi-kilometer-long THz links can become a reality [8]. *Hence, the use of highly-directional antennas becomes de-facto mandatory for prospective THz communications in 6G and beyond-6G networks.*

The use of highly-directional THz antennas however brings its own challenges. *First*, besides the complexity and associated costs, these high-gain antennas also make THz communication system even more vulnerable to possible beam blockage, as most of the transmitted energy gets concentrated over a unique narrow path [9], [10]. As most common objects, including human bodies (i.e., other people around the user), significantly attenuate THz signals, *blockage mitigation* becomes one of the essential challenges to address in THz systems [11], [12].

Second, high-gain antennas typically feature large electrical apertures. As the aperture size D increases, so does the extent of the near-field region, delimited by the Fraunhofer distance: $2D^2/\lambda$ [13]. Given the submillimeter wavelengths at THz frequencies, the near-field region can extend surprisingly far, even with cm-scale physical apertures. For instance, a 15-cm aperture at 300 GHz has a near-field region of *up to 45 meters*. This raises the real possibility that users in a wireless area network can be predominantly located in the near-field region of a THz access point.

This realization has sparked extensive research into the effects of operating in the near-field region at THz frequencies [14]–[20]. While challenges such as non-planar wavefronts and near-field beam squint exist [21], numerous advantages can be exploited. We have recently pointed out the possibility of engineering exotic optics-inspired wavefronts that have no equivalent in the far-field [15]. These wavefronts include focused beams that can locally increase the energy at specific locations, as well as Bessel beams capable of reconstructing themselves after blockage ("*self-healing*") [22].

Furthermore, we introduced the class of self-accelerated beams for near-field communications at THz frequencies [23]. This class includes Airy and caustic beams which possess the intriguing property of following curved trajectories as they propagate in the near-field. In particular, we experimentally showed that these beams can evade obstacles in the line-of-sight, making them a promising solution to blockage [24].

Given the vast possibilities offered by near-field wavefront engineering and self-accelerated beams specifically, it is crucial to develop numerical techniques for effective benchmarking. One fundamental aspect to consider is to ensure that sufficient power is delivered to the receiver. While in typical far-field scenarios, the Friis equation is used to establish link budgets, there is no direct equivalent of the notion of antenna

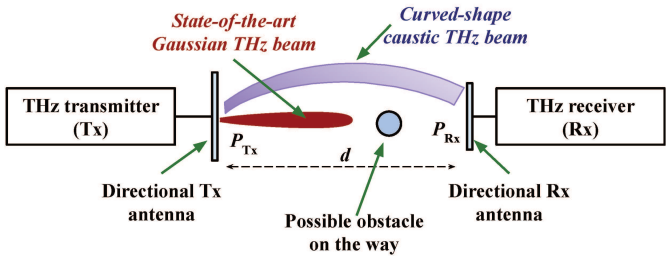

Fig. 1. High-level representation of the modeled scenario consisting of a single THz transmitter (Tx) and a single THz receiver (Rx). While the highly directional Gaussian beam is susceptible to blockage, the curved-shape caustic beams can go around the obstacle.

gains in the near-field when employing self-accelerated beams.

This paper presents a numerical methodology to calculate the received power reaching a receiver located in the near field when the transmitter uses a self-accelerated Airy beam to *"curve the THz signal around an obstacle"*. Fig. 1 shows a high-level representation of the modeled scenario. The setup consists of a single THz transmitter (Tx) and a single THz receiver (Rx). The THz transmitter is equipped with a directional antenna that can transmit THz signal at frequency f with total transmit power P_{Tx}. The receiver side is also equipped with a directional antenna aligned with the Tx one. The Tx and Rx THz antennas are separated from each other by a given distance of d meters.

Our previous work employed a semi-analytical method to compute near-field patterns [25]. However, that approach was limited to scenarios without obstacles in the beam path or to regions in close proximity to the transmitter. The new methodology introduced in this paper overcomes the abovementioned limitations, allowing us to investigate the effect of any number and type of obstacles placed in the near-field, with the receiver positioned at any point in space.

The rest of the paper is organized as follows. In Section II, we briefly review how to engineer trajectories in the near-field using self-accelerated beams. In Section III, we show how to obtain the near-field link budget, which combines the use of a commercial solver along with post-processing calculations. Next, Section IV provides an example of a calculation that compares a caustic beam to a Gaussian beam in the presence of an obstacle. Finally, to demonstrate the capabilities of our numerical methodology, we perform a statistical analysis of the performance of caustic beams in the presence of obstacles.

II. Trajectory Engineering of Self-Accelerated Beams

Self-accelerated beams possess the ability to propagate along curved trajectories in the near-field. To engineer the trajectory, we consider a ray optics approach and the concept of caustics [18]. Consider the geometry depicted in Fig. 2, where we aim to generate the trajectory defined by the red curve. Caustics are defined along the trajectory. Shown in green, these correspond to the set of lines that intersect the trajectory at the tangents. These caustics make an angle θ with the input axis: $\tan(\theta) = dg(z)/dz$. For a point $(z_i, g(z_i))$ of index i on the trajectory, the corresponding caustic line is given by:

$$c_i(z) = \left.\frac{dg(z)}{dz}\right|_{z=z_i} z + g(z_i) - \left.\frac{dg(z)}{dz}\right|_{z=z_i} z_i \tag{1}$$

From the generalized Snell's law [26], one can then find the required phase profile at the input plane to realize the desired trajectory:

$$\phi(x) = \frac{2\pi}{\lambda}\int \frac{dg(z)/dz}{\sqrt{1+(dg(z)/dz)^2}}dx \tag{2}$$

Using this method, any convex function (where caustics intersect the trajectory only once at the tangent) can be achieved.

Fig. 2 depicts an example of a trajectory engineered using this method along with the corresponding simulated near-field electric field distribution. In this example, the trajectory is of equation $x(z) = 0.19\sqrt{z}$ and leads to a nonlinear phase distribution that can be calculated from (2). In our simulation, this phase distribution is used at the input plane as an excitation source, and has the form: $\exp(-j\phi(x))$. In practice, these apertures can be realized in many ways, for example using metasurfaces or phase plates [24]. The main idea is to impose a phase distribution of the form given by (2).

However, there are also limitations on the curvature of the trajectory caused by the finite aperture size. Indeed, for two points on the trajectory, $(z_1, g(z_1))$ and $(z_2, g(z_2))$, the necessary aperture size D is directly related to the distance between where the caustics intersect the input plane following:

$$D = \left| \left(g(z_2) - \left.\frac{dg(z)}{dz}\right|_{z=z_2} z_2 \right) - \left(g(z_1) - \left.\frac{dg(z)}{dz}\right|_{z=z_1} z_1 \right) \right| \tag{3}$$

This essentially means that a large input aperture is required to realize a trajectory with a tight curvature.

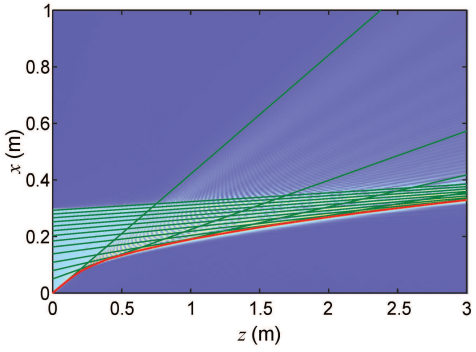

Fig. 2. Construction of a caustic beam using ray optics overlapping the corresponding simulated electric field. The caustics (in green) are tangent to the intended trajectory (in red).

III. Near-Field Link Budget Calculation

In standard far-field situations, link budgets are calculated with the Friis equation, an equation that describes the amount of power received relative to the transmit power. This equation reads:

$$\frac{P_{\mathrm{Rx}}}{P_{\mathrm{Tx}}} = G_{\mathrm{Tx}}(\theta,\phi)G_{\mathrm{Rx}}(\theta,\phi)\left(\frac{\lambda}{4\pi d}\right)^2 \tag{4}$$

Here, d is the distance between the transmitter and the receiver antennas. It is interesting to note that the gains of the receiver and transmitter are typically expressed using only the angular spherical coordinates θ and ϕ, while the radial coordinate is assumed to be part of the free-space path loss term: $(\lambda/4\pi d)^2$. Indeed, in far-field situations and under the Friis equation, waves decrease in power with the distance following $1/d^2$. While the Friis equation provides an elegant method for computing link budgets using intrinsic characteristics of antennas independent of distance (i.e., antenna gains), this equation is not applicable in the near-field since 1) there is no direct equivalent of antenna gains in the near-field, and 2) powers do not necessarily drop monotonically with distance. This last point can be fairly understood when considering focused beams in which powers increase (at the focal plane) before decreasing.

Therefore, to compute link budgets in the near-field, one has to resort to computing the electric field at the receiver location. In this work, we use the finite element method to numerically obtain the field emitted from a transmitter aperture, at any position in space. This method has the advantage of allowing us to also simulate the presence of obstacles.

From the fields obtained from the numerical simulations, we can compute the transmitted and received powers. In general, the power traversing an aperture S (in free space) is calculated from the radiated electric field at the aperture location $E(x,y)$ as [27]:

$$P = \frac{1}{2Z_0}\iint_S |E(x,y)|^2 \mathrm{d}S \tag{5}$$

where $Z_0 = 377\ \Omega$ is the free-space impedance. Using (5), we first compute the power at the receiver aperture P_{Tx}. This will serve as the normalization factor $P_{\mathrm{Rx}}/P_{\mathrm{Tx}}$ in the link budget.

As for the power on the receiver aperture (P_{Rx}), it can be computed as:

$$P_{\mathrm{Rx}} = \frac{\eta}{2Z_0}\iint_S |E(x,y)|^2 \mathrm{d}S \tag{6}$$

Equation (6) is similar to (5), with the addition of the power coupling efficiency η. This factor (a number between 0 and 1) describes how much energy is effectively coupled into the receiver. To compute the coupling efficiency, we can use a mode coupling approach [28]:

$$\eta = \frac{\iint_S E(x,y,z)\cdot E_{\mathrm{Rx}}\mathrm{d}S}{\sqrt{\iint_S |E(x,y)|^2\mathrm{d}S}\sqrt{\iint_S |E_{\mathrm{Rx}}(x,y)|^2\mathrm{d}S}} \tag{7}$$

where all the integrals are evaluated over the receiver aperture. Here, E_{Rx} is the receiver's radiated field when operated as a transmitter. By the antenna reciprocity principle, the coupling efficiency is maximized (i.e., $\eta \to 1$) when the transmitter field is geometrically superimposed (in amplitude, phase and polarization) to the receiver antenna field.

IV. Numerical Results

Using the methodology described above, we now present numerical results comparing the performance of caustic beams to conventional highly directional Gaussian beams. Subsection IV-A provides a detailed example of a calculation based on our methodology, while showcasing the superior performance of caustic beams when an obstacle is placed in the beam path. In subsection IV-B, we extend the analysis and perform a comparative statistical study for randomly placed obstacles to identify the conditions under which caustic beams perform better.

A. Evasion capabilities of caustic beams

Our illustrative scenario considers a 30-cm transmitter aperture positioned in the $z = 0$ plane. The receiver, located 3 meters away, has a 60 mm aperture spanning from $x = 0.32$ m to $x = 0.38$ m (depicted by a red line in Fig. 3a and b). A circular metallic obstacle, 90 mm in diameter, is placed 50 cm from the input aperture (white circle in Fig. 3a and b).

Figs. 3a and b show the simulated 300-GHz radiated electric field for the caustic and Gaussian beam respectively. Here, the Gaussian beam is steered towards the receiver at a 3.8-degree angle, corresponding to the axis between the centers of the transmitter and receiver apertures. In contrast, the caustic beam is designed to circumvent the obstacle, by following the analytical trajectory $g(z) = 0.19\sqrt{z}$, where $g(z)$ and z are expressed in meters. Using (2), we numerically find the phase distribution at the input aperture capable of reproducing this trajectory.

As can be seen, the presence of the obstacle greatly blocks the Gaussian beam's electric field, whereas the caustic beam easily propagates around it. This is further confirmed in Fig. 3c where the electric field distribution on the $z = 3$ m plane is shown. There, the two vertical dashed lines correspond to the receiver aperture. For comparison, we also reproduced simulations without the obstacle, depicted as dotted lines in Fig. 3c. The results show that the caustic beam's electric field at the receiver position remains virtually unaffected by the obstacle's presence, whereas the Gaussian beams's amplitude is substantially reduced.

From these electric field distributions, we can compute the power at the receiver aperture using the integrals shown in (5) and (6), assuming a normalized transmitter output of 0 dBm. Without any obstacle, we observe that the caustic beam captures -2.05 dBm of power, while the Gaussian beam collects -6.82 dBm of power. The difference between the two highlights the focusing effect of caustic beams. When an obstacle is introduced, the received power for the caustic beam experiences a minimal change (-2.06 dBm), however,

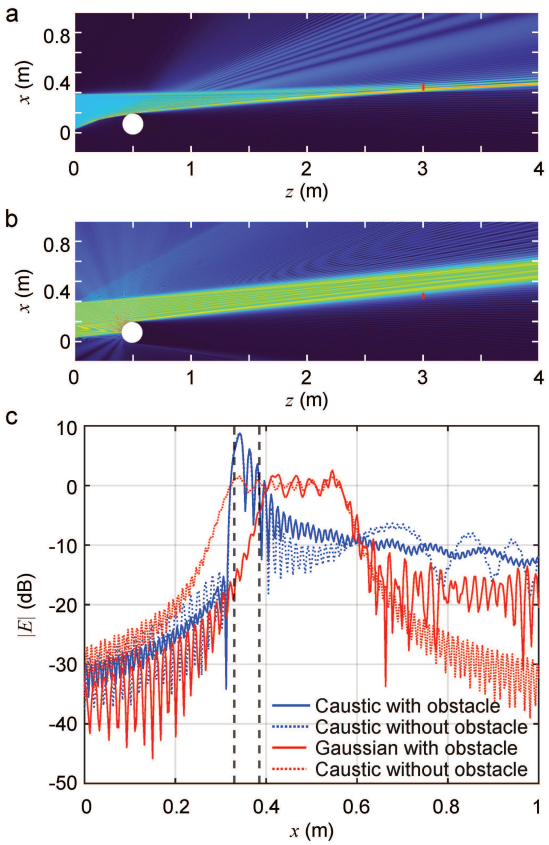

Fig. 3. (a) Electric field distribution in the presence of an obstacle in the beampath for the caustic and (b) the Gaussian beam. (c) Electric field amplitude at a distance $z = 3$ m away from the transmitter, for the caustic (blue) and Gaussian (red) beam in the presence (solid line) and absence (dotted line) of an obstacle. The vertical dashed lines correspond to the position of the receiver.

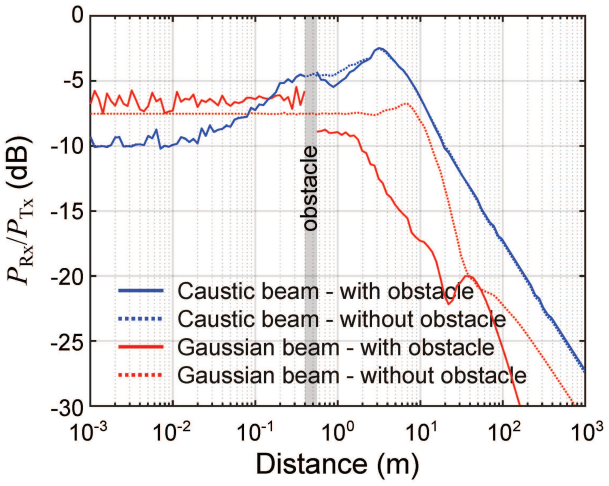

Fig. 4. Received power as a function of distance for the caustic (blue) and Gaussian (red) THz beams, in the presence (solid line) and absence (dotted line) of an obstacle between the THz transmitter and THz receiver antennas.

the Gaussian beam significantly reduces to -18.46 dBm. These results confirm the superior performance of the caustic beam in the presence of obstacles.

We can reproduce the calculation for any receiver location in space. Figure 4 presents the results when the receiver is moved up to 1 km away from the transmitter, for both the cases of caustics (blue) and Gaussian (red). The simulation is reproduced with (solid line) and without (dashed line) the obstacle. Again, the caustic beam (blue) remains virtually unaffected by the presence of the obstacle, as shown by the nearly identical dashed and sold blue lines. This confirms the caustic beam's ability to circumvent the obstacle effectively, even in the far-field. In contrast, the Gaussian beam experiences a significant power reduction in the near-field (1-10 meter region) when the obstacle is present. This power reduction is also observed in the far-field. Furthermore, the caustic beam exhibits a focusing behavior with power increasing up to a distance of 3 meters before declining. This characteristic contrasts with the Gaussian beam, which maintains relatively constant power before reducing.

B. Statistical analysis

In this section, we present an advanced statistical analysis of the blockage mitigation capabilities of caustic beams. In our analysis, we consider the geometry previously described: a 300-mm receiver and a 60-mm receiver located 3 meters away. However, this time, we position the metallic obstacle at a random position between the transmitter and receiver. The obstacle's center position is derived from a uniform probability distribution in a rectangular region between the transmitter and receiver. Fig. 5a shows the empirical probability density function (pdf) for the link budget (effectively, P_{Rx}/P_{Tx}) for obstacle radii of 1, 40 and 75 mm (green, orange and red histograms respectively). In Fig. 5b, we show the average received power as a function of the obstacle radius, with the standard deviations shown as error bars.

First, we note that the simulation results for the caustic beam generally cluster closer to 0 dB compared to those of the Gaussian beam. This is due to the focusing effect of caustic beams, which increases the received power even in the absence of obstacles. As a function of the radius size, we observe that the smaller obstacle radius (1 mm) minimally affects received power probability. This is because the obstacle is very small in relative to the transmitter size, allowing sufficient power to still reach the receiver. However, as obstacle size increases, the probability distribution extends towards negative values, with higher probability of negative values for the Gaussian beam. This indicates that, overall, the caustic beam outperforms the Gaussian beam in the presence of obstacles.

To further analyze the data, Fig. 6 presents the simulations when distributed in space. For each obstacle position, we compute the received power difference (in dB) between the caustic and Gaussian beams, plotting it spatially as a colored dot with a gradient from blue to red. Here, red (positive difference) indicates superior caustic performance, while blue

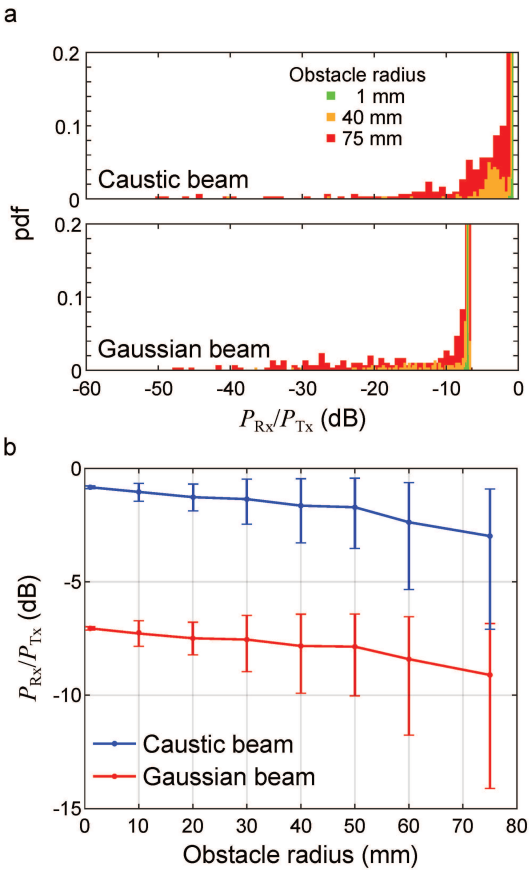

Fig. 5. Histograms comparing the received power of the caustic beam (top) with the Gaussian beam (bottom) when the obstacle is positioned randomly (300 simulations per histogram). (b) Average values of the received power as a function of the obstacle size, for the caustic (blue) and Gaussian (red) beam. *The error bars correspond to the standard deviation.*

(negative difference) signifies higher received power for the Gaussian beam.

In general, for all radius sizes, most points have pink values, particularly for obstacle positions not directly between the transmitter and receiver. Again, this occurs due to the energy-focusing ability of caustic beams, which outperform Gaussian beams even without obstacles in the beam path.

For the smaller radius (30 mm), there is no blue dots, indicating that the caustic beam consistently outperforms the Gaussian beam. As obstacle size increases, the graph shows greater effectiveness of the caustic beam, with dots becoming redder, especially below the theoretical trajectory. Interestingly, for larger obstacle sizes (60 and 75 mm), we observe blue dots near the receiver, indicating superior Gaussian performance in these situations. These points correspond to the focal point of the caustic beam. When a sufficiently large obstacle is placed there, it can completely block the focused radiation. In general, these results confirm the ability of caustic beams to effectively mitigate blockage caused by objects in the beam path.

V. Conclusion

In this paper, we explored and analyzed a novel feature of near-field THz communications – the ability to effectively mitigate blockage by "curving the THz signal around obstacles". Particularly, we developed a numerical methodology combining the use of a finite-element method solver with post-processing integral calculations as an efficient method to evaluate the performance of such a system. Addressing the lack of approach to estimate the performance of these beams in the THz near field in the presence of obstacles, our proposed methodology can simulate the effect of an obstacle and receiver placed anywhere in between the THz transmitter and the THz receiver antennas.

We then used this tool to compare the performance of a caustic and a Gaussian beam (produced by i.e., conventional THz beamforming) in mitigating the blockage events. Through a statistical analysis of our simulated results, we showed that the caustic beam consistently outperforms Gaussian beams when obstacles are present, providing up to 20 dB gain in the receiver power (so up to 100 times more energy captured by the THz receiver). Analyzing the results of this study, we do believe that, *first*, the developed evaluation methodology and the derived results may be further extended and thus serve as a building block toward modeling more complex 3D scenarios for (beyond-)6G THz communications with mobility of nodes, imperfect beam alignment, etc. *Second*, our promising first-order findings suggest that caustic THz beams – and the more general class of self-accelerated beams – can be an important tool to realize more reliable THz communications in forthcoming practical deployment scenarios vulnerable to blockage by various type of real obstacles.

VI. Acknowledgement

H. Guerboukha acknowledges funding support from the US National Science Foundation (NSF-2402784). V. Petrov acknowledges the support from Digital Futures and Grant 2022-04222 from the Swedish Research Council (VR).

References

[1] A. Shafie, N. Yang, C. Han, J. M. Jornet, M. Juntti, and T. Kürner, "Terahertz communications for 6G and beyond wireless networks: Challenges, key advancements, and opportunities," *IEEE Network*, vol. 37, p. 162–169, May 2023.

[2] T. Kürner, D. M. Mittleman, and T. Nagatsuma, *THz Communications: Paving the Way Towards Wireless Tbps*. Springer Nature, Dec 2021.

[3] M. Z. Chowdhury, M. Shahjalal, S. Ahmed, and Y. M. Jang, "6G wireless communication systems: Applications, requirements, technologies, challenges, and research directions," *IEEE Open Journal of the Communications Society*, vol. 1, p. 957–975, 2020.

[4] S. Jia, L. Zhang, S. Wang, W. Li, M. Qiao, Z. Lu, N. M. Idrees, X. Pang, H. Hu, X. Zhang, L. K. Oxenlowe, and X. Yu, "2 × 300 Gbit/s line rate PS-64QAM-OFDM THz photonic-wireless transmission," *Journal of Lightwave Technology*, vol. 38, p. 4715–4721, Sep 2020.

[5] H. Sasaki, Y. Yagi, R. Kudo, and D. Lee, "Demonstration of 1.44 Tbit/s OAM multiplexing transmission in sub-THz bands," in *2023 IEEE International Conference on Communications Workshops (ICC Workshops)*, IEEE, May 2023.

[6] Keysight, "6G: Going beyond 100 Gbps to 1 Tbps," *White Paper*, Oct 2022.

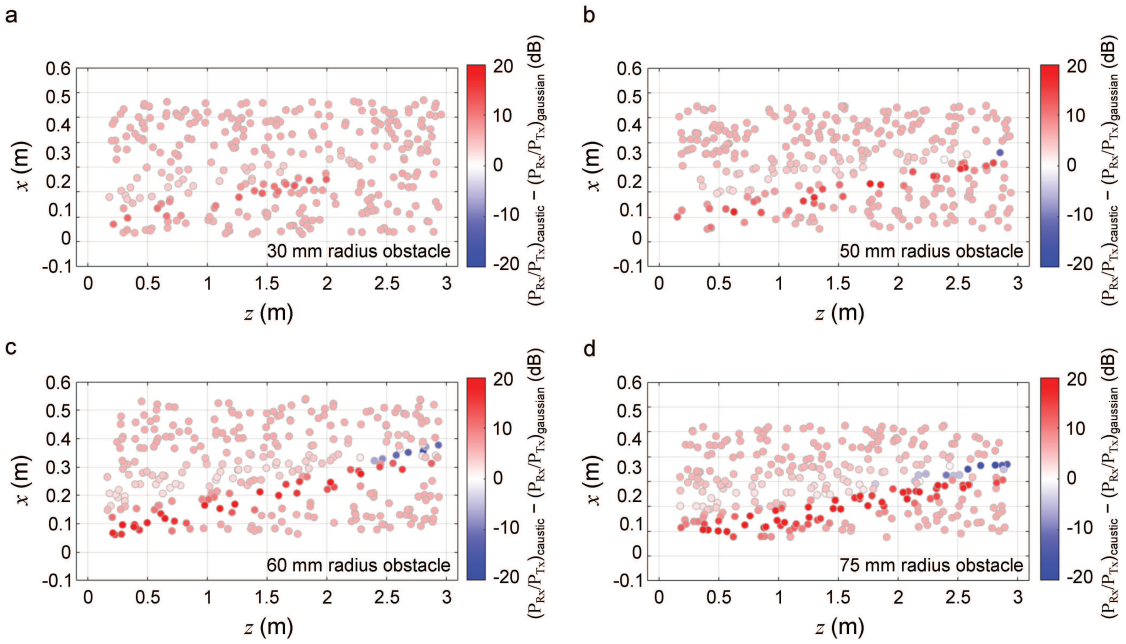

Fig. 6. Difference in received power between the caustic beam and the Gaussian beam for different obstacle positions, and for various obtacle radii: (a) 30 mm, (b) 50 mm, (c) 60 mm, and (d) 75 mm. The dot corresponds to the obstacle position, while its color encodes the value of the power difference with red and blue corresponding respectively to positive (caustic outperforms Gaussian) and negative (Gaussian outperforms caustic) difference.

[7] H. Guerboukha, R. Shrestha, J. Neronha, O. Ryan, M. Hornbuckle, Z. Fang, and D. M. Mittleman, "Efficient leaky-wave antennas at terahertz frequencies generating highly directional beams," *Applied Physics Letters*, vol. 117, Dec 2020.

[8] P. Sen, J. V. Siles, N. Thawdar, and J. M. Jornet, "Multi-kilometre and multi-gigabit-per-second sub-terahertz communications for wireless backhaul applications," *Nature Electronics*, vol. 6, p. 164–175, Dec 2022.

[9] R. Vannithamby and A. Soong, *5G Verticals: Customizing Applications, Technologies and Deployment Techniques*. Wiley–IEEE Press, 2020.

[10] J. Kokkoniemi, J. Lehtomäki, V. Petrov, D. Moltchanov, and M. Juntti, "Frequency domain penetration loss in the terahertz band," in *2016 Global Symposium on Millimeter Waves (GSMM) & ESA Workshop on Millimetre-Wave Technology and Applications*, pp. 1–4, June 2016.

[11] C. Chaccour, M. N. Soorki, W. Saad, M. Bennis, P. Popovski, and M. Debbah, "Seven defining features of terahertz (THz) wireless systems: A fellowship of communication and sensing," *IEEE Communications Surveys & Tutorials*, vol. 24, pp. 967–993, Jan 2022.

[12] V. Petrov, M. Komarov, D. Moltchanov, J. M. Jornet, and Y. Koucheryavy, "Interference analysis of EHF/THF communications systems with blocking and directional antennas," in *2016 IEEE Global Communications Conference (GLOBECOM)*, pp. 1–7, December 2016.

[13] C. A. Balanis, *Antenna theory: Analysis and design*. John Wiley & Sons, 2016.

[14] V. Petrov, D. Bodet, and A. Singh, "Mobile near-field terahertz communications for 6G and 7G networks: Research challenges," *Frontiers in Communications and Networks*, vol. 4, Mar 2023.

[15] A. Singh, V. Petrov, H. Guerboukha, I. V. Reddy, E. W. Knightly, D. M. Mittleman, and J. M. Jornet, "Wavefront engineering: Realizing efficient terahertz band communications in 6G and beyond," *IEEE Wireless Communications*, vol. 31, p. 133–139, Jun 2024.

[16] M. Cui, Z. Wu, Y. Lu, X. Wei, and L. Dai, "Near-field MIMO communications for 6G: Fundamentals, challenges, potentials, and future directions," *IEEE Communications Magazine*, vol. 61, p. 40–46, Jan 2023.

[17] A. Singh, V. Petrov, and J. M. Jornet, "Utilization of Bessel beams in wideband sub terahertz communication systems to mitigate beamsplit effects in the near-field," in *ICASSP 2023 - 2023 IEEE International Conference on Acoustics, Speech and Signal Processing (ICASSP)*, IEEE, Jun 2023.

[18] C. Han, Y. Chen, L. Yan, Z. Chen, and L. Dai, "Cross far- and near-field wireless communications in terahertz ultra-large antenna array systems," *IEEE Wireless Communications*, vol. 31, p. 148–154, Jun 2024.

[19] V. Petrov, D. Moltchanov, and J. M. Jornet, "Accurate channel model for near field terahertz communications beyond 6G," in *2024 IEEE 25th International Workshop on Signal Processing Advances in Wireless Communications (SPAWC)*, pp. 781–785, September 2024.

[20] K. Rouhi, S. E. Hosseininejad, S. Abadal, M. Khalily, and R. Tafazolli, "Multi-channel near-field terahertz communications using reprogrammable graphene-based digital metasurface," *Journal of Lightwave Technology*, vol. 39, p. 6893–6907, Nov 2021.

[21] W. Hao, X. You, F. Zhou, Z. Chu, G. Sun, and P. Xiao, "The far-/near-field beam squint and solutions for THz intelligent reflecting surface communications," *IEEE Transactions on Vehicular Technology*, vol. 72, p. 10107–10118, Aug 2023.

[22] I. V. Reddy, D. Bodet, A. Singh, V. Petrov, C. Liberale, and J. M. Jornet, "Ultrabroadband terahertz-band communications with self-healing Bessel beams," *Communications Engineering*, vol. 2, Oct 2023.

[23] H. Guerboukha, B. Zhao, E. Knightly, and D. M. Mittleman, "Curved Airy-Like beams for terahertz wireless communications," in *CLEO 2023*, (Washington, D.C.), Optica Publishing Group, 2023.

[24] H. Guerboukha, B. Zhao, Z. Fang, E. Knightly, and D. M. Mittleman, "Curving THz wireless data links around obstacles," *Communications Engineering*, vol. 3, Mar 2024.

[25] H. Guerboukha, B. Zhao, Z. Fang, E. Knightly, and D. M. Mittleman, "Curving THz beams in the near field: A framework to compute link budgets," in *Proc. of the 18th European Conference on Antennas and Propagation (EuCAP)*, IEEE, Mar 2024.

[26] N. Yu, P. Genevet, M. A. Kats, F. Aieta, J.-P. Tetienne, F. Capasso, and Z. Gaburro, "Light propagation with phase discontinuities: Generalized laws of reflection and refraction," *Science*, vol. 334, p. 333–337, Oct 2011.

[27] N. Llombart and S. O. Dabironezare, "Feasibility study of quasi-optical MIMO antennas for radiative near-field links," *IEEE Transactions on Antennas and Propagation*, vol. 70, p. 7073–7083, Aug 2022.

[28] K. Nallappan, H. Guerboukha, Y. Cao, G. Xu, C. Nerguizian, D. M. Mittleman, and M. Skorobogatiy, *Terahertz Waveguides for Next Generation Communication Network*, p. 379–410. New York: CRC Press, Jun 2021.